# Acoustic imaging of objects buried in soil

Catherine H. Frazier[a)]
*Bioacoustics Research Laboratory and Department of Electrical and Computer Engineering, University of Illinois at Urbana-Champaign, Urbana, Illinois 61801*

Nail Çadallı[b)] and David C. Munson, Jr.[c)]
*Coordinated Science Laboratory and Department of Electrical and Computer Engineering, University of Illinois at Urbana-Champaign, Urbana, Illinois 61801*

William D. O'Brien, Jr.[d)]
*Bioacoustics Research Laboratory and Department of Electrical and Computer Engineering, University of Illinois at Urbana-Champaign, Urbana, Illinois 61801*

(Received 17 May 1999; accepted for publication 13 March 2000)

In this study, we demonstrate an acoustic system for high-resolution imaging of objects buried in soil. Our goal is to image cultural artifacts in order to assess in a rapid manner the historical significance of a potential construction site. We describe the imaging system and present preliminary images produced from data collected from a soil phantom. A mathematical model and associated computer software are developed in order to simulate the signals acquired by the system. We have built the imaging system, which incorporates a single element source transducer and a receiver array. The source and receiver array are moved together along a linear path to collect data. Using this system, we have obtained *B*-mode images of several targets by using delay-and-sum beamforming, and we have also applied synthetic aperture theory to this problem. © *2000 Acoustical Society of America.* [S0001-4966(00)00207-1]

PACS numbers: 43.35.Pt [HEB]

## INTRODUCTION

Once a cultural or archeological resource site is identified, it must be assessed in order to determine its significance and eligibility for National Registry of Historic Places (Executive Order 11593). Current methods for this assessment involve scattered small-scale digs at the site, which are expensive and imprecise. The cost of complete assessments is prohibitive; therefore, there is an urgent need to significantly reduce the cost of data recovery, especially for the many sites having lower probabilities of containing significant cultural or archeological resources. This study proposes an acoustic system for high-resolution imaging of buried artifacts, within this context.

In addition to finding cultural artifacts, a system designed to image buried objects could be adapted to detect land mines. However, a system built for detecting artifacts can look straight down, while a system for finding land mines must have side-looking capability. There is currently a world-wide effort to reduce the harm caused to local populations by unexploded ordnance. Acoustic and electromagnetic systems have been proposed to meet this purpose. Land mines can be metallic or plastic, and they range in size. A small anti-personnel mine can be as small as 50 mm. Electromagnetic systems have detection/identification problems due to the air/ground interface, which reflects much of the incident energy, and other objects such as rocks and ammunition shells or other metal fragments, which are difficult to distinguish from mines.[1,2] In practice, up to one thousand metal fragments are found for every one mine.[3] Despite this, land mines may be easier to detect than cultural artifacts because land mines are often larger than artifacts and they have greater reflectivity due to larger impedance mismatch with soil.

An acoustic system has potential advantages over existing imaging modalities. Current technologies in seismic exploration and borehole techniques are not designed to meet the resolution requirements for imaging cultural artifacts or land mines. In 1990, a study showed that, using acoustic techniques for subsurface imaging, resolution could be improved from tens of meters achievable in petroleum and mineral exploration to on the order of 1 meter using geophysical tomography (boreholes) for applications such as finding buried waste or abandoned mines.[4] However, finding cultural artifacts will require resolution on the order of 5 cm.

Ground penetrating radar (GPR) has had some success in identifying underground structures; however, the success is site specific, depending on the moisture content of the soil.[5] In Ref. 6, a comparison was made between GPR and the seismic reflection method for shallow geological surveys to a depth of 50 m. They showed that GPR was effective in dry soil, but that water attenuated the electromagnetic energy. Conversely, acoustic energy propagated better in a saturated medium than in dry soil. Thus, an acoustic system would complement a GPR system.

At the same time our system was being developed, Smith *et al.*[7] developed an acoustic system for localizing reflections from a buried object on a natural beach. They used a shaped pulse, as does our system, rather than impulse excitation. The center frequency of their transmitted pulse was

[a)]Electronic mail: hillsley@brl.uiuc.edu
[b)]Electronic mail: cadalli@dsp.csl.uiuc.edu
[c)]Electronic mail: d-munson@uiuc.edu
[d)]Electronic mail: wdo@uiuc.edu

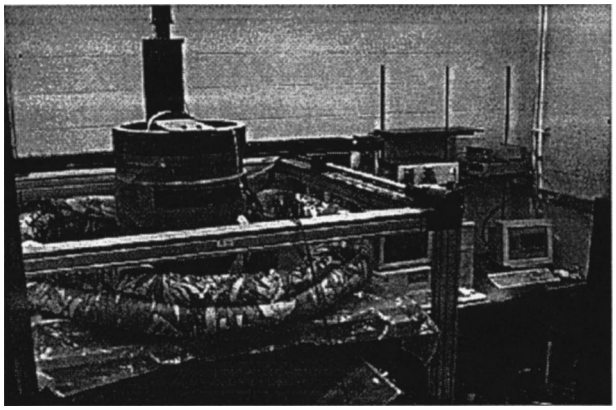

FIG. 1. Experimental system.

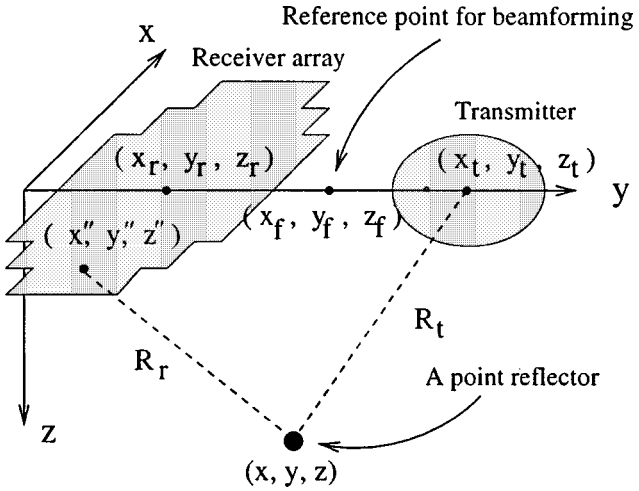


FIG. 2. Array of transducers and associated coordinate system. Surface of the array is in the *x*-*y* plane. Array motion is in the *y* direction.

100 Hz, and they considered propagating distances up to 10 m. Our system is intended to be used up to a maximum depth of 1 m and to detect smaller objects; therefore, we propagate a much higher frequency pulse. The main disadvantage in Smith's system is that it requires subtracting a background image, with no targets present, making it an impractical system for use in a situation where data are not taken before targets are placed.

In this paper, we present a system that demonstrates the feasibility of acoustically imaging small objects buried in dry homogeneous soil. This paper is organized as follows: In the next section we describe the experimental system. The characteristics of the soil used in our tests are presented in Sec. II. Section III introduces the data model. Section IV explains the methods we used for image reconstruction and presents images reconstructed from both simulated and real data. Further research directions are listed in Sec. V.

## I. EXPERIMENTAL SYSTEM

Our imaging system has been constructed and is in operation at the U.S. Army Construction Engineering Research Laboratory (CERL) in Champaign, Illinois, where the data are collected in a controlled volume of soil. A picture of the system is shown in Fig. 1. The soil is contained in a cubic wooden box of 1.2 m per side. The box has a false bottom, with only the top 60 cm filled with soil. The system incorporates a torpedo transducer array from the Applied Research Laboratory at Pennsylvania State University. The torpedo head, which contains the receiver array, is suspended above the box by a metal frame that surrounds the box. The source is to the right of the torpedo head. Sitting on top of the box of soil is a child's pool filled with 3 cm depth of water. The water is used to couple the sound energy between the transducers and the sand since the transducers are designed for underwater applications. To the right of the frame are two computers. The left computer is used to control the motion of the receiver array along three translational axes. The right computer controls the data acquisition, including communication with the motion control computer.

The source transducer is a single element that is well approximated as a point source. In future versions of the system, we hope to use a transmitter array to provide focusing of the transmit beam to increase the energy coupled into a localized volume of soil, thereby improving signal-to-noise ratio. In the torpedo head, a 52-element sonar array ($8\times8$, 3.56 $cm^2$ close-packed elements with 3 elements in each corner missing) serves as the receive array, and allows for beamforming on receive. The receiver array and the corresponding coordinate system are depicted in Fig. 2. The *z* axis represents the depth into the soil and the *x*-*y* plane represents the soil surface. The *y* and *z* dimensions are called azimuth and range, respectively. The detailed geometry of the transmitter and the receiver is shown in Fig. 3. Due to the size of the torpedo and the source, the smallest possible center-to-center spacing of the source and receive array is 33 cm.

A block diagram of the system is shown in Fig. 4. Movement of the array is accomplished by a motion control system with three translational axes. Only the two horizontal axes, with positional accuracy of 3 $\mu$m, were used for the scans. Position control is achieved through a PC-based control card using LabView software to create the interface. The motion control program allows manual positioning or automatic control by the data acquisition computer, which uses the serial port to send position coordinates to the motion control computer.

The data acquisition computer uses an Hewlett Packard

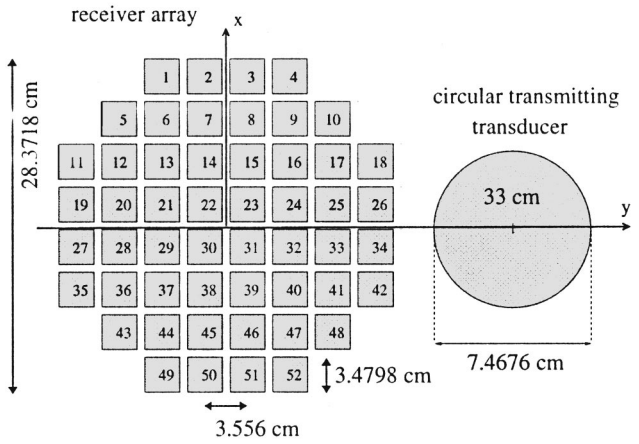


FIG. 3. Geometry of the transmitter and receiving array; view from the top. Origin is at the center of the receiver array.

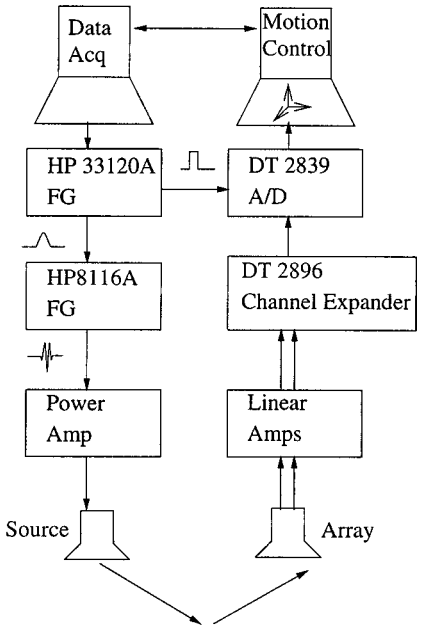


FIG. 4. Block diagram of imaging system.

Interface Bus (HPIB) interface card to communicate with the HP33120A function/arbitrary waveform generator to set up initial parameters for the excitation signal. The excitation signal is generated by the function/arbitrary waveform generator modifying the signal (AM modulation) from an HP8116A pulse/function generator. The resulting signal is a cosine-weighted pulse of 6 cycles at 6 kHz which is plotted in Fig. 5. The choice of center frequency was influenced by the operational requirements of the acoustic transducers and by resolution considerations. Achievable resolution is determined in part by the medium. Propagation speed determines the wavelength for a given frequency. With a higher frequency, better resolution can be achieved; however, higher frequencies suffer from large attenuation resulting in poor signal-to-noise ratio. The signal was amplified by either a 3000-W amplifier (Industrial Test Equipment Co.) or a 1000-W amplifier with variable output impedance capability (Instruments, Inc. Model L10).

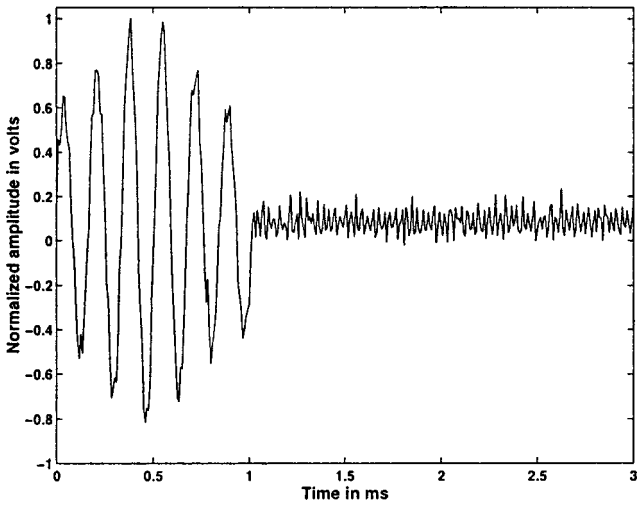


FIG. 5. Transmitted signal.

Signals from the 52 elements were captured individually so that processing could be done off-line. Received signals were averaged 64 times. A separate transmit pulse was used for each signal captured, so that at each position of the source and receiver array, 3328($52\times64$) pulses were transmitted. Before the received signal was digitized, it was amplified by an in-line linear amplifier with a gain of 330.

The synchronization signal from the HP33120A was used to trigger data collection by the Data Translation A/D board (DT 2839, 12 bit, 1 MHz). The DT 2839 has 8 channels, so we used a DT 2896 channel expander (Data Translation) to allow us to capture the 52 channels individually.

## II. SOIL PROPERTIES

The soil was gathered from the University of Illinois Sand Farm in Mason County, Illinois. Physical characterization of the soil was performed by University of Illinois Professor Robert Darmody, a certified soil classifier by the Illinois Soil Classifiers Association. The sand content was 94%, most of which was evenly divided between the medium (250–500 $\mu$m) and fine (100–250 $\mu$m) sand subclasses. Because of the low clay content, the soil was nonplastic. Organic carbon content was low, as was the soil moisture.

Acoustic properties of soil are described by the Biot theory for sound propagation in a porous medium.[8,9] The theory predicts the propagation of two compressional waves and a shear wave in the porous medium. The first compressional wave is characterized by particle motion in phase with the fluid motion. The second compressional wave is characterized by particle motion out of phase with the fluid motion. The first wave is often referred to as the fast compressional wave because it generally has a higher speed than the wave of the second type, or slow compressional wave. Also, the slow compressional wave generally has much higher attenuation than the fast compressional wave. The velocity of the shear wave is determined by the shear modulus of the solid. For materials such as clays, silts or muds, the velocity may be much slower than either compressional wave. The attenuation of the shear wave may be larger or smaller than the attenuation of the fast wave. In our experiments, the Biot fast wave was the only wave detected, which was a result of the high attenuation of the slow wave, and more importantly, the coupling conditions, which led to the preferential coupling of energy into the fast wave.

The wave speed and attenuation of the propagated wave were determined using the experimental system described above. The source and receiver were positioned above a steel plate buried at a depth of 12 cm. The 6 kHz center frequency pulses described previously were transmitted and received at the 52 elements. The array was then moved an additional 2 cm away from the source and the data collection was repeated. Data were collected for a total of five positions of the array in increments of 2 cm. This data collection differs from the data collection for images, where the relative positions of the source and receiver remained fixed.

The total distance traveled by the pulse was calculated using geometric acoustics. It was assumed that the speed of sound was constant in the first 12 cm of sand, so the sound traveled over a linear path from the source to the plate and

from the plate to the receiver element. The sound speed was measured by correlating the signal received by each element with the signal received by the same element after the array had been moved to a different position. The difference in pulse travel distance was then divided by the difference in time of arrival. Results showed that the speed of sound in the sand was $166 \pm 27$ m/s.

Attenuation was measured by first finding the log power spectrum of the received signals. The first position of the array was used as a reference for comparison with the four other positions. The log decrements for the four positions were calculated and fitted to a line for each of the 52 elements, so that the slopes of the lines give 52 estimates of the attenuation per cm at a particular frequency. The average slope, where the average was taken over the 52 estimates, was then taken to be the attenuation in dB/cm at that frequency. Finally a line was fit to the data for the range of frequencies. The results showed that for our sand, the attenuation was approximately 0.65 (dB/cm)/kHz in the frequency range from 500 Hz to 2 kHz. We did not receive a useful signal above 2 kHz so we could not extend attenuation measurements to higher frequencies. A larger soil characterization study performed in the Bioacoustics Research Laboratory measured speed of sound and attenuation of the fast compressional wave over the range of frequencies, 1–10 kHz, for six soil types as a function of four soil moistures and two soil compactions using through transmission methods.[10] The study showed that speed of sound and attenuation for all samples varied over small ranges, 100–300 m/s and 0.1–1 dB/cm kHz, respectively.

Our results are in general agreement with the results for unconsolidated sand by Hickey and Sabatier.[11] They measured a phase velocity of 143 m/s for the slow wave and 240 m/s for the fast wave. The slow wave attenuation was measured to be 3.0 dB/cm at 1 kHz and the fast wave attenuation was measured to be 0.87 dB/cm at 1 kHz. In their experiments, both phase velocity and attenuation of the slow wave increased with frequency.

## III. DATA ACQUISITION MODEL

We have developed a mathematical model and associated computer software to simulate the signals acquired by the experimental system. Our simulator serves as a convenient platform for the development of image reconstruction algorithms. In our model, the medium (soil) is assumed to consist of densely spaced point scatterers, which are placed on a three-dimensional grid, representing the object(s) and the soil background. Each scatterer is assigned a reflection coefficient $\Gamma_0(x,y,z)$, with magnitude $m(x,y,z)$ and phase $\theta(x,y,z)$.

In considering the returned signal, let us first deal with the case of one scatterer. The received response from a particular reflector is a delayed version of the transmitted signal scaled by the reflection coefficient of the scatterer and by a factor which is dependent on the range function and which is due to the attenuation of the medium and the radial expansion of the spherical wave.[12] The transmitted signal is $\mathrm{Re}\{s(t)e^{j2\pi f_0 t}\}$ where $s(t)$ is a baseband pulse and $f_0$ is the carrier frequency.

Receiving element surfaces are considered to be decomposed into a collection of point receivers. Since the transmitting element is approximately omnidirectional, such a decomposition is not necessary for that element. For a particular scatterer, the signal received at a transducer is the sum of the signals received by those point receivers on the surface of the transducer. This model accounts for the curvature of the wavefront incident on the transducer and eliminates the need for the knowledge of the receiving transducer beam pattern. In reference to Fig. 2, let us denote the coordinates of a point scatterer by the vector $\mathbf{v}=(x,y,z)$. Similarly, we denote the center locations of the transmitter and the receiver array by $\mathbf{v}_t=(x_t,y_t,z_t)$ and $\mathbf{v}_r=(x_r,y_r,z_r)$, respectively. Notice that for the case when the transmitter and the receiver array are in the $x$-$y$ plane and move along the $y$ axis, we have $\mathbf{v}_t=(0,y_t,0)$ and $\mathbf{v}_r=(0,y_r,0)$. The signal received by the $i$th receiver, when the transmitter is at $\mathbf{v}_t$ and the center of the receiver array is at $\mathbf{v}_r$, is

$$\tilde{g}_i(t_1,\mathbf{v}_t,\mathbf{v},\mathbf{v}_r)=\int\int w_i(x'',y'';\mathbf{v}_r)m(x,y,z)\times\mathrm{Re}\left\{s\left(t-\frac{R(\mathbf{\Lambda})}{c}\right)e^{j[2\pi f_0(t-R(\Delta)/c+\theta(x,y,z)]}\right\}\times\frac{e^{-gaR(\mathbf{\Lambda})}}{R_t(\mathbf{v}_t,\mathbf{v})R_r(\mathbf{v}'',\mathbf{v})}dx''dy''. \quad (1)$$

Here $\mathbf{v}''=(x'',y'',z'')$ is the coordinate of the simple receiver on the surface of the $i$th receiver transducer. If the receiver array is in the $x$-$y$ plane, $z''=0$. This surface is represented by the window function $w_i(x'',y'';\mathbf{v}_r)$, the location of which depends on the position of the array center, $\mathbf{v}_r$. Vector $\Lambda=[\mathbf{v}\mathbf{v}_t\mathbf{v}''\mathbf{v}_r]$ is defined for notational simplicity. The attenuation coefficient of the medium (in units of $\mathrm{m}^{-1}$) is $\alpha$ and $c$ is the speed of sound in soil. The range function $R(\Lambda)$ is the sum of $R_t(\mathbf{v}_t,\mathbf{v})$, which is the distance from the transmitter to a particular scatterer, and $R_r(\mathbf{v}'',\mathbf{v})$, which is the distance from the scatterer to the infinitesimal receiver surface on a particular receiver transducer. $R_t$ and $R_r$ are given as

$$R_t(\mathbf{v}_t,\mathbf{v})=\sqrt{(x-x_t)^2+(y-y_t)^2+(z-z_t)^2},$$
$$R_r(\mathbf{v}'',\mathbf{v})=\sqrt{(x-x'')^2+(y-y'')^2+(z-z'')^2}. \quad (2)$$

The integrand in Eq. (1) is a delayed version of the transmitted signal reflected from a scatterer at $\mathbf{v}$. It is scaled by the magnitude of the reflectivity and phase shifted by the phase of the reflectivity. The fractional term in the integrand is the attenuation term. The numerator of this term represents the attenuation due to the medium and the denominator accounts for the attenuation due to the spherical expansion of the acoustic wave. The return wave is incident onto a point receiver at the coordinate $\mathbf{v}''$. The limits of the integration are determined by $w_i(x'',y'';\mathbf{v}_r)$. Hence, the integration is over the surface of the $i$th receiver transducer.

After quadrature demodulation, we have the complex baseband representation of the received signal as

$$\overline{g_i}(t,\mathbf{v}_t,\mathbf{v},\mathbf{v}_r)=\int\int w_i(x'',y'';\mathbf{v}_r)\Gamma_0(x,y,z)\times\frac{e^{-\alpha R(\Lambda)}}{R_t(\mathbf{v}_t,\mathbf{v})R_r(\mathbf{v}'',\mathbf{v})}\cdot s\left(t-\frac{R(\Lambda)}{c}\right)\times e^{-jkR(\Lambda)}dx''dy'', \quad (3)$$

where $k=2\pi f_0/c$ is the wavenumber. The term due to attenuation can be eliminated approximately by using time gain compensation (TGC) on the received data.[13] The total received signal for the $i$th transducer of the receiver array, for a fixed array position is the sum of responses from all scatterers in the medium:

$$\hat{g}_i(t,\mathbf{v}_t,\mathbf{v}_r)=\int_0^\infty\int_{-\infty}^{\infty}\int_{-\infty}^{\infty}\overline{g_i}(t,\mathbf{v}_t,\mathbf{v},\mathbf{v}_r)dxdydz. \quad (4)$$

In computer implementation of this model, it is not possible to account for a continuum of scatterers or a semi-infinite medium. Therefore we assume a finite size, three-dimensional, discrete grid of point scatterers in order to simulate objects and the background soil.

## IV. IMAGE RECONSTRUCTION

By translating the receiver array across the surface of the medium, it is possible to obtain sufficient data to form an image of the soil subsurface. The data acquisition system is moved along a straight line, and at regular spatial intervals the system emits the tapered sinusoidal pulse and collects returns. We mainly have explored two methods of forming images from the collected data, as explained below. Reconstructed images represent the *y*-*z* plane at a fixed *x* value according to our coordinate convention in Fig. 2.

### A. Beamforming and experimental results

At each position of the data acquisition system, a single beam can be formed by focusing the array broadside, so that a conventional *B*-mode image may be formed with data from multiple positions. Alternatively, since the signals have been recorded separately, several beams can be formed for each source/receiver array position by synthesizing several elements centered at positions between the source and the receiver. To synthesize an element between the source and receiver, the 52 signals are first delayed to simulate a signal transmitted from a synthesized position, and then are delayed to simulate a focused receiver at the synthesized position. Creating multiple beams at each position of the source and receiver could provide for some averaging to increase signal-to-noise ratio, although this was not done in our study.

Focusing of the 52 individual received signals is accomplished off-line through delay-and-sum beamforming, using dynamic focusing so that multiple depths in the image are in focus. The lateral resolution is not constant as a function of depth, due to the fixed size of the array. As stated earlier, the coordinates $(x'',y'',z'')$ in Fig. 2 are used to designate the position of a simple receiver on the $i$th receiver. For this discussion, we will use the coordinates $(x_i,y_i,0)$, where $(x_i,y_i)$ is the center of the $i$th receiver element. The subscript $i$ varies from 1 to 52 and is used to enumerate the elements. The center of the array lies on the $x$ axis so that half of the elements are in the region where $x>0$ and half are in the region where $x<0$. The source is centered at position $(0,y_t,0)$, and the synthetic element is centered at $(0,y_f,0)$. In our case, the synthetic element is both transmitter and receiver. The reason for using such synthesized elements in delay computation rather than using one of the receive elements as a reference for the others is to utilize the shortest path length traveled by the transmitted signal for a particular depth so as to reduce the effect of attenuation.

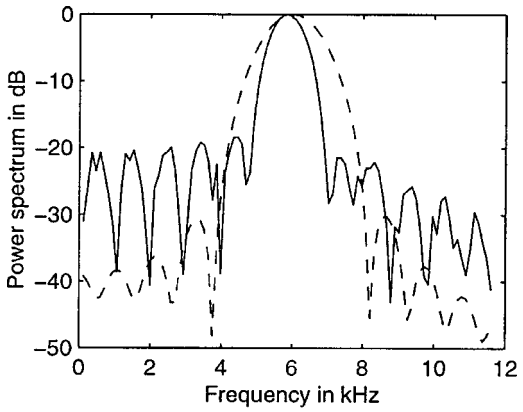


FIG. 6. Log spectra of simulated (dashed) and actual (solid) transmitted signals.

For a desired focal point, $(0,y_f,z_f)$, where the focal point is always directly below the synthetic element, the beamforming is accomplished as follows:

$$t_t=(z_f-\sqrt{(y_t-y_f)^2+z_f^2})/c, \quad (5)$$

$$t_{ri}=(z_f-\sqrt{x_i^2+(y_f-y_i)^2+z_f^2})/c, \quad (6)$$

$$g(t)=\sum_{i=1}^{52}s_i(t-t_t-t_{ri}). \quad (7)$$

The delay, $t_t$, is the same for each element. It compensates for the difference in travel time from the actual source to the focal point and from the synthetic source to the focal point. The delay, $t_{ri}$, is different for each element. It compensates for the difference in travel times from the focal point to the actual receivers and from the focal point to the synthetic receiver. The $g(t)$ are envelope-detected using the Hilbert Transform and displayed side-by-side to form an image.

Data were collected using a variety of targets. In each case, the source and receiver array were moved in 0.5-cm steps. The information about the targets was contained in frequencies below 1500 Hz rather than near 6 kHz, which was the center frequency of our transmit pulse. The received signal contained a strong signal at 6 kHz; however, this was most likely reverberation within the pool. The high received signal strength at frequencies below 1500 Hz can be explained as follows. In the transmitted signal, the energy at frequencies below 2 kHz is 20 dB below the center frequency, as shown in Fig. 6. The attenuation in the soil was measured to be 0.65 (dB/cm)/kHz for the frequencies be-

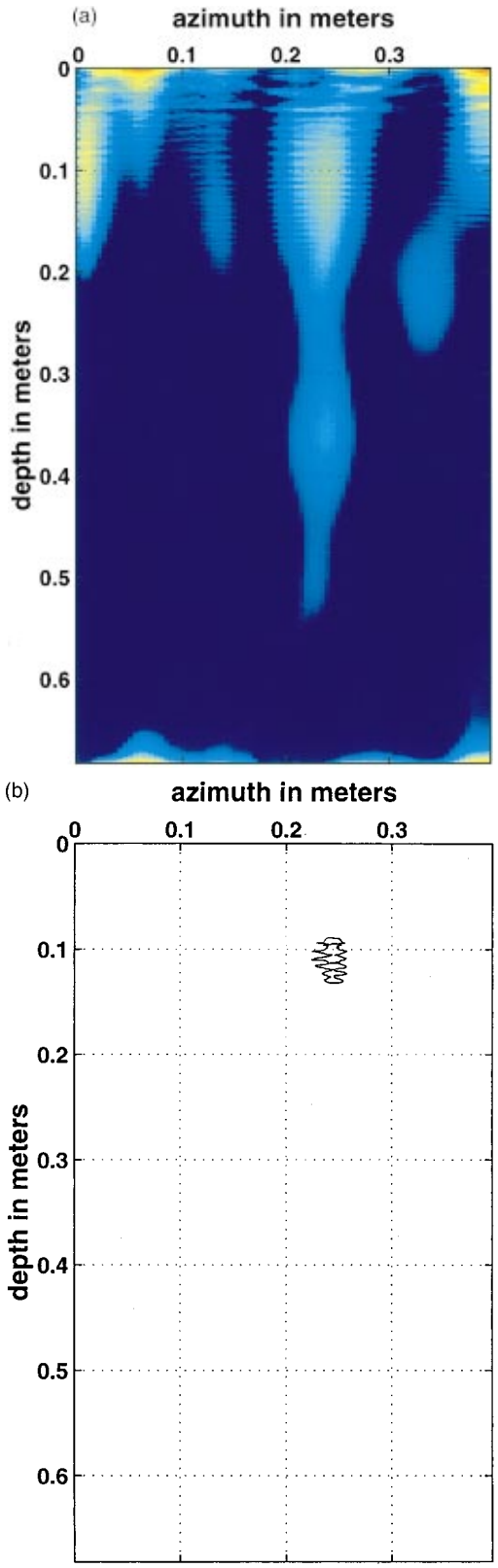


FIG. 7. (a) Image of air-filled furnace pipe. The axis of the pipe is perpendicular to the page. The reflection due to the pipe is centered at approximately 0.24 meters in azimuth and 0.12 meters in depth. (b) Contour plot showing the location of the target in the image.

tween 500 Hz and 2 kHz. The pulse typically must travel 40 cm from the source to the target to the receiver element. In this distance, the 6 kHz signal would be attenuated 156 dB, assuming that the attenuation measurement can be extended to this high frequency. The 500 Hz signal would be attenuated just 13 dB. Therefore, low frequencies should be more prominent in the received signal.

The delay and sum imaging algorithm was modified so that the DC bias of the signal received at each element was removed before any further calculations. The second step in processing the data was to filter the signals such that only frequencies below 1500 Hz were kept, because the SNR is poor at high frequencies.

A reconstructed image of a single target is shown in Fig. 7. Part (b) of the figure shows the location of the target in the image. The target was an air-filled aluminum furnace pipe (7.5-cm diameter, 90-cm length) buried at a depth of 8.5 cm. The pipe appears as the bright spot centered between 0.2 and 0.3 m in azimuth and between 0.1 and 0.2 m in depth. The bright spots in the corners are due to reflections from the sides of the box. The bright spot beneath the pipe, between 0.3 and 0.4 m in depth is due to a multiple reflection. The image was formed by synthesizing an element 8 cm from the center of the array.

A reconstructed image with multiple targets is shown in Fig. 8. Part (b) of the figure shows the location of the five targets in the image. The image shows resolution targets buried at approximately 9-cm depth. The resolution targets were 5 bars with center-to-center spacings of 3.7, 6.2, 8.8, and 10.1 cm. Each bar was $1.2\times7.5\times60$ cm with the longest dimension perpendicular to the scan, and the smallest dimension parallel to the scan. The total width of the target cluster was 30 cm. The data were focused by forming a synthesized element at a position 2.5 cm from the center of the array. The first bar appears at the left of the image (between 0 and 0.1 meters in azimuth) and is less bright than the others. Two bars appear between 0.1 and 0.2 m in azimuth. The second bar appears small and is difficult to distinguish. The third bar is centered at approximately 0.15 meters in azimuth and 0.15 meters in depth. The remaining bars are those with the largest separations and are bright targets in the image. One is centered at approximately 0.24 m in azimuth and 0.14 m in depth. The other is centered at approximately 0.38 m in azimuth and 0.1 m in depth. The predicted axial resolution is 16 cm at best, as calculated from the pulse duration and the speed of sound in the soil.

Figure 9 shows a second image with multiple targets. The soil contained three buried objects: two bottles, and a metal bar, $70\times10\times1$ cm. The bar was buried 6 cm deep so that the lateral dimension was 1 cm and the axial dimension was 10 cm. The bottles were buried end to end so that at the position where the source and array passed over them, they behaved as an air-filled glass tube, 7 cm in diameter and 30-cm long. They were buried 11.5-cm deep. Part (b) of the figure shows the locations of the bar and bottles in the image. The bar appears on the left, and the bottles appear on the right. The image was formed by synthesizing a single element at the position of the receiver array. In this image, the metal bar appears as the bright spot centered at approximately 0.14 m in azimuth and 0.15 m in depth. The spot immediately to the right of it is a side lobe. The spots below the metal bar are due to multiple reflections. The bottles

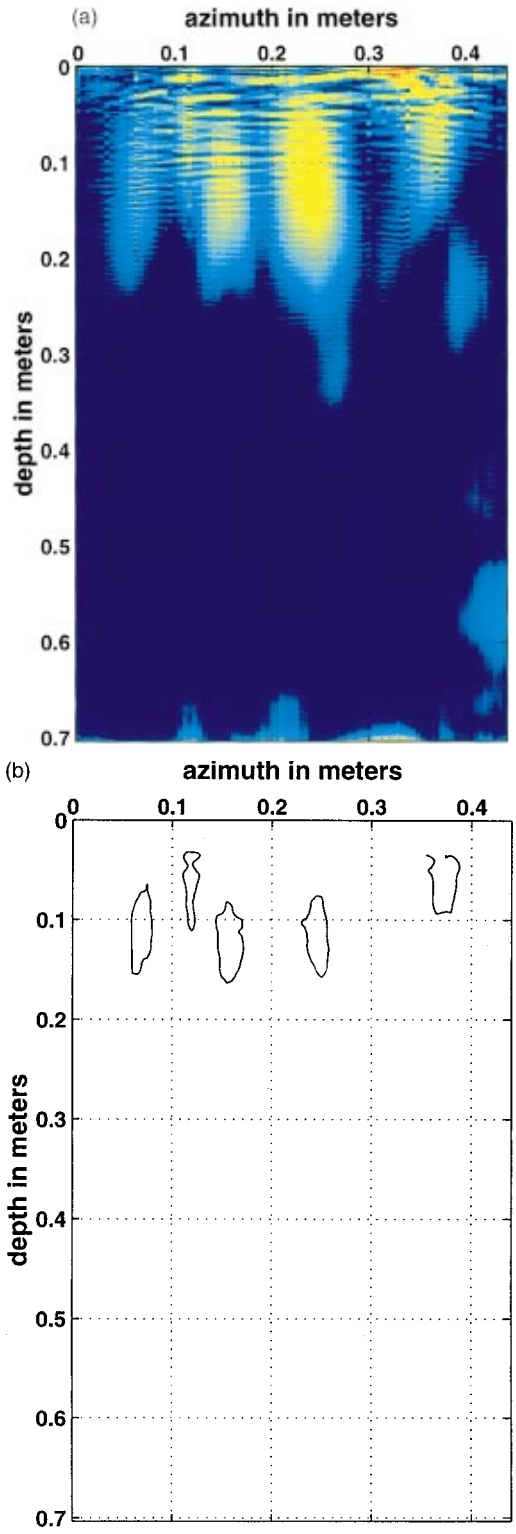


FIG. 8. (a) Image of resolution target. The resolution target consists of 5 parallel metal bars with increasing center-to-center separation (3.7, 6.2, 8.8, and 10.1 cm). It is difficult to distinguish the second and third bars in the image. In the image, the reflections due to the bars are centered at (0.05, 0.15), (0.11, 0.05), (0.15, 0.15), (0.24, 0.14) and (0.38, 0.1), where the first coordinate is the azimuth, the second coordinate is the depth, and both coordinates are given in meters. (b) Contour plot showing the locations of the metal bars in the image.

appear as a spot located approximately 0.38 meters in azimuth and 0.15 meters in depth. We conclude from this image that solid targets give a stronger reflection than do air-filled targets.

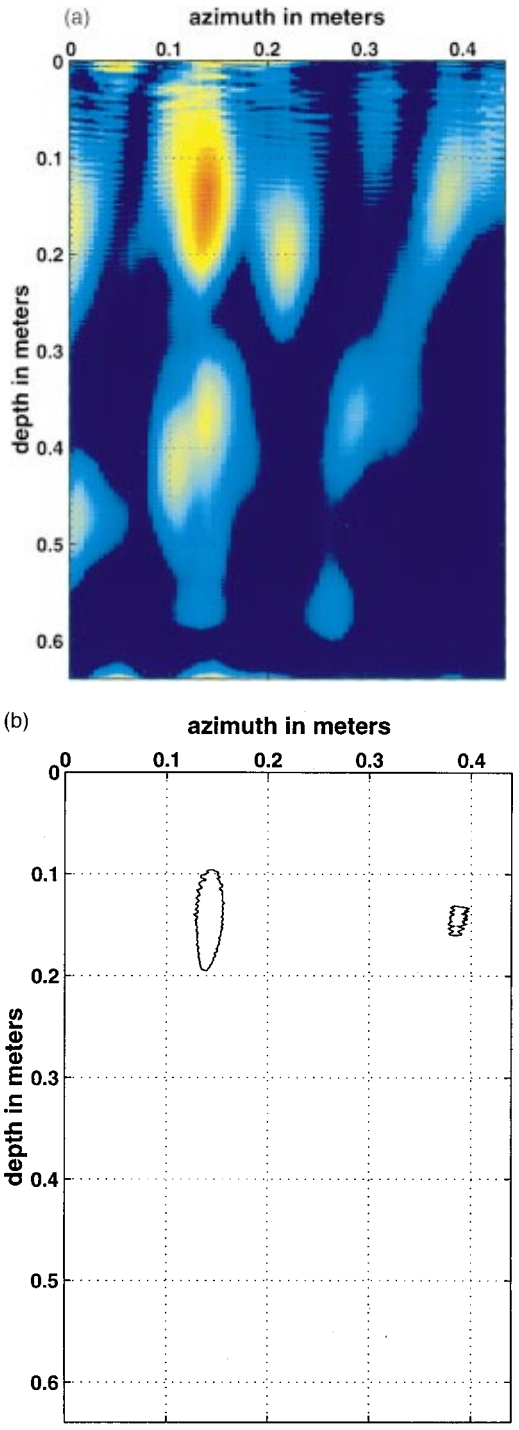


FIG. 9. (a) *B*-mode reconstructed image of metal bar and bottles using real data. The reflection due to the metal bar is centered at 0.14 meters in azimuth and 0.16 meters in depth. The reflection due to the bottles is centered at 0.38 meters in azimuth and 0.13 meters in depth. (b) Contour plot showing the locations of the targets in the image.

### B. Synthetic aperture approach and simulation results

Given $N$ transducers, a linear receiver array could provide far higher resolution than a rectangular array if synthetic aperture processing were used. Suppose data were collected from a linear array moved in a direction normal to its orientation. This corresponds to a linear array with its longer dimension being along the $x$ axis as depicted in Fig. 10. High resolution in the direction of travel could then be obtained by

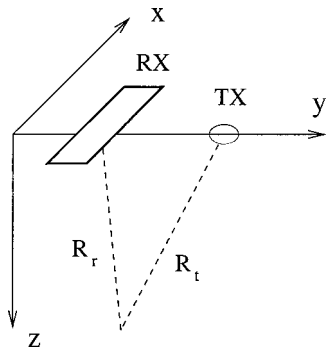


FIG. 10. Linear array and off-center transmitter.

using algorithms similar to those employed in synthetic aperture radar (SAR) or synthetic aperture sonar. High resolution along the dimension of the array would be obtained by using the beamforming approaches described above. A difference between subsurface imaging and SAR is that in the former we have attenuation of the signal due to the medium. We have developed a SAR-type reconstruction algorithm for the acoustic imaging scenario using a modification of the correlation algorithm described in Refs. 14 and 15. The main steps and the necessary modifications are explained briefly in the following.

By passing the returned signal through a quadrature demodulator, the carrier can be suppressed and the complex baseband signal can be obtained for each of the receivers in the linear array. The linear array then can be focused to a fixed depth, or can be dynamically focused to various depths by using beamforming. This results in a single waveform for each location of the data acquisition system. Let us denote the signal obtained after focusing as

$$\overline{g}(t,y_a)=\int_{-\infty}^{\infty}\int_{-\infty}^{\infty}\Gamma_0(y,z)w_a(y-y_a)w_r(z)\times s\left(t-\frac{R_t+R_r}{c}\right)e^{jk(R_t+R_r)}dy\,dz, \tag{8}$$

where $y_a$ is the azimuth coordinate at which the returns are collected by the linear receiver array. $w_a(y)$ and $w_r(z)$ are window functions representing the area illuminated by the transmitted acoustic beam in the azimuth and range directions, respectively. First-order Taylor approximations of $R_r$ and $R_t$,

$$R_r=\sqrt{(y-y_a)^2+z^2}\approx z+\frac{(y-y_a)^2}{2z}, \tag{9}$$

$$R_t=\sqrt{(y-y_a-d)^2+z^2}\approx z+\frac{(y-y_a-d)^2}{2z}, \tag{10}$$

are valid if the conditions $z\gg y-y_a$ and $z\gg y-y_a-d$ hold. Here, $d$ is the distance between the transmitter and receiver. We assume that the transmitted signal varies slowly enough that $s(t-(R_t+R_r)/c)\approx s(t-2z/c)$. Assigning $\Gamma(y,z)=\Gamma_0(y,z)e^{-j2kz}$ and making the change of variables, $y\to\nu$, and $z\to\xi$, and $t=2z/c$, we can write

$$g(y_a,z)=\int\overline{\Gamma}(y_a,\xi)w_r(\xi)s\left(\frac{2}{c}(z-\xi)\right)d\xi \tag{11}$$

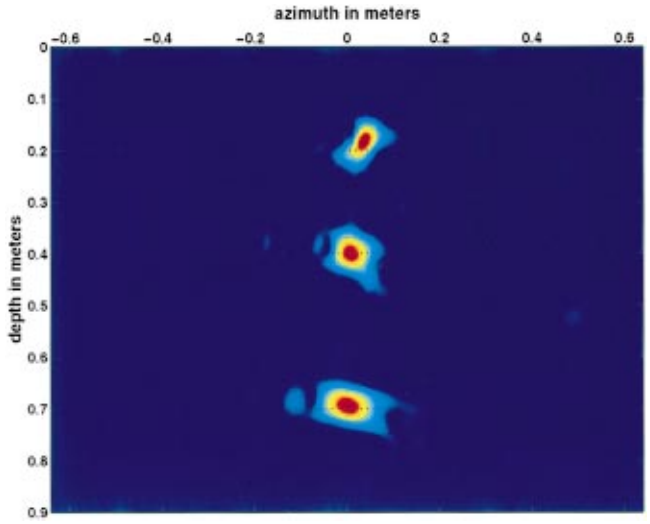


FIG. 11. SAR-type reconstruction of three point objects from simulated data.

$$\overline{\Gamma}(y_a,\xi)=\int\Gamma(\nu,\xi)w_a(\nu-y_a)\exp\left(-jk\frac{(\nu-y_a)^2}{2\xi}\right)\times\exp\left(-jk\frac{(\nu-y_a-d)^2}{2\xi}\right)d\nu. \tag{12}$$

In the so-called range processing step, the received signal in Eq. (11) is correlated with the transmitted signal to find a matched-filter estimate for $\overline{\Gamma}(y_a,z)$. Then this estimate is used to solve for $\overline{\Gamma}(y_a,z)$ by correlating the estimate of $\overline{\Gamma}(y_a,z)$ with the filter corresponding to the exponential terms in Eq. (12). This step is called azimuth processing. With the above formulation, range processing is the same as in the standard correlation-based SAR algorithm in Ref. 14. But in the standard algorithm, since it has been derived for a radar scenario, there is only one signal received by the single antenna located on the radar platform. Also, for the case of a single antenna, the transmitter-to-reflector and reflector-to-receiver distances are the same in the radar case. Notice that the attenuation term in Eq. (1) is not incorporated in Eq. (8). This is because we apply time-gain compensation to the received signal to compensate approximately for the effect of attenuation.

The above SAR-type algorithm was applied to simulated data consisting of three point targets and background soil scatterers. A linear array of 8 receivers, corresponding to the center of the experimental receiver array, were used. The point targets were positioned at $x=y=0$ and at depths 0.1 m, 0.4 m, 0.7 m. The grid for the background soil scatterers extended from $x=-0.2$ m to $x=0.2$ m, from $y=-0.49$ m to $y=0.49$ m, and from $z=0.01$ m to $z=0.9$ m. The resulting image is shown in Fig. 11. As mentioned, we used time-gain compensation to nearly eliminate the effect of attenuation. Without the compensation, only the scatterer at $z=0.1$ could be seen. Note that the point objects are not reconstructed at their correct locations in depth. This effect is most noticeable for the object closest to the surface. The reason for this is that our Taylor approximations for the transmitter-reflector-receiver distances are not valid for close objects. In a SAR

scenario, these approximations generally are valid because the range distance in radar imaging is typically very large. Note also that we approximated two distance functions in our case to take into account the off-center transmitter. If the standard monostatic SAR algorithm had been applied without that modification, the point target images in Fig. 11 would have been shifted in the azimuth direction, too. The clouds around the images of point objects are due to the soil scatterers.

In a SAR reconstruction, resolution in the range direction increases as the bandwidth of the transmitted signal increases. Azimuth resolution depends on the distance covered by the data acquisition system during illumination of a target by the transmitted acoustic beam. Collecting more data in the azimuth dimension provides for an increase in resolution in the azimuth direction. In our experimental system, the length of the scan is limited by the size of the box, which presented a complication to successfully applying SAR-type imaging. In addition, it may be necessary to apply autofocus techniques[16] to successfully form images from experimental data.

## V. CONCLUSIONS AND FURTHER RESEARCH

An acoustic approach was described for imaging objects buried in soil, with the primary purpose of detecting and imaging cultural artifacts. An experimental system was designed and implemented. Also, a mathematical model and associated computer software were developed in order to simulate the signals acquired by the actual system. Subsurface images were reconstructed from real and simulated data by using delay-and-sum beamforming and by the application of synthetic aperture theory.

We have shown that our acoustic system can successfully detect objects buried in soil. Targets spaced 5 cm apart can be resolved as separate objects. Targets with a cross section as small as 1.2 cm by 7.5 cm can be seen as long as they have sufficient length.

The images clearly show targets; however, there is also much clutter which needs to be identified and removed. *B*-mode images could be improved by modifying the processing. First, apodization weights could be applied to the receiver array elements to reduce sidelobes. This modification should remove effects such as those due to the sides of the box in the image of the pipe. Second, we could form small images at each position of the source and receiver and then average the images from different transducer positions to create the final image with an improved signal-to-noise ratio. As discussed previously, we could create these small images by synthesizing multiple elements between the source and receiver.

The system itself could be improved to produce data with better signal-to-noise ratio. Currently we use a point source and array receiver. The source and receiver were chosen because of their availability and their ability to transmit high powered, shaped pulses and to receive small signals. With a focused source, we could transmit more energy to the region of interest, rather than spreading the energy over a wide area. In addition, if we could put the source and receiver closer together, we could increase the depth of penetration by reducing the total distance the sound must travel from source to target to receiver at a given depth. Our source had been designed to give the best performance between 6 kHz and 10 kHz. We actually used received signal components at a lower frequency, so another improvement would be to use a source with an optimal response at 2 kHz or even below. Also, work has already begun on developing transducers better matched to the impedance of soil.

We must be able to see smaller targets in order to use the system to detect cultural artifacts. Currently we can detect objects with small cross-sectional area and significant length. By moving the source and receiver in two dimensions rather than along a linear path, we would be more likely to detect small objects.

Finally, the system must be moved from the laboratory to the outdoors, where the actual use of the system will occur. Besides testing the equipment in a more realistic environment with a nonhomogeneous soil sample, this would allow us to collect data over a longer scan, making synthetic aperture approaches more appropriate. Wave-number–domain SAR algorithms, which are expected to give more accurate results for near-field sources, can then be tested.[17,18] In order to bring the system outside, a new mechanism for holding the transducers will be necessary as well as a new means of coupling the acoustic energy to the soil. Most likely, the transducers will be mounted on a vehicle. One possibility is to mount multiple transducers on a cylinder which is then rotated across the soil surface. Water coupling, using the child's pool, could be used in initial outdoor tests, but this would limit the total length of the scan. A final system will not have its transducer impedance matched to water, so coupling through a thin layer of air should be possible, although further investigation will be necessary. Coupling through air will change the boundary conditions, resulting in more energy coupled into the slow Biot wave.

This research was supported by the U.S. Army Construction Engineering Research Laboratory under Contract DACA88-96 K 0002.

[1] L. J. Carter, G. H. Bryant, M. LeFevre, and W. C. Wong, ''Moisture and land mine detection,'' in *Proceedings of the EUREL International Conference on the Detection of Abandoned Land Mines: A Humanitarian Imperative Seeking a Technical Solution*, Edinburgh, UK, Edinburgh International Conference Centre, Oct. 7–9, 1996, pp. 83–87.

[2] A. Langman and M. R. Inggs, ''A stepped frequency cw polarimetric radar for mine detection,'' in *Proceedings of the EUREL International Conference on the Detection of Abandoned Land Mines: A Humanitarian Imperative Seeking a Technical Solution* (Ref. 1), pp. 109–113.

[3] R. J. Chignell, ''Ground penetrating radar: A sensor for mine detection,'' in *Proceedings of the EUREL International Conference on the Detection of Abandoned Land Mines: A Humanitarian Imperative Seeking a Technical Solution* (Ref. 1), pp. 103–108.

[4] A. J. Witten and W. C. King, ''Acoustic imaging of subsurface features,'' J. Env. Eng. **116**, 166–181 (1990).

[5] L. Peters, Jr., J. J. Daniels, and J. D. Young, ''Ground penetrating radar as a subsurface environmental sensing tool,'' Proc. IEEE **82**, 1802–1822 (1994).

[6] D. M. McCann, P. D. Jackson, and P. J. Fenning, ''Comparison of seismic and ground probing radar methods in geological surveying,'' IEE Proc. F, Radar Signal Process. **135**, 380–390 (1988).

[7] E. Smith, P. S. Wilson, F. W. Bacon, J. F. Manning, J. A. Behrens, and T. G. Muir, ''Measurement and localization of interface wave reflections from a buried target,'' J. Acoust. Soc. Am. **103**, 2333–2343 (1998).

[8] M. A. Biot, ''Theory of propagation of elastic waves in a fluid saturated porous solid. I. low-frequency range,'' J. Acoust. Soc. Am. **28**, 168–178 (1956).
[9] M. A. Biot, ''Theory of propagation of elastic waves in a fluid saturated porous solid. II. high-frequency range,'' J. Acoust. Soc. Am. **28**, 179–191 (1956).
[10] W. D. O'Brien, Jr. and R. G. Darmody, ''Acoustic characterization of soil,'' Soil Sci. Soc. Am. J. (submitted).
[11] C. Hickey and J. Sabatier, ''Measurements of two types of dilatational waves in an air-filled unconsolidated sand,'' J. Acoust. Soc. Am. **102**, 128–136 (1997).
[12] A. D. Pierce, *Acoustics: An Introduction to Its Physical Principles and Applications* (McGraw-Hill, New York, 1981).
[13] K. K. Shung, M. B. Smith, and B. M. W. Tsui, *Principles of Medical Imaging* (Academic, San Diego, 1992).
[14] D. C. Munson, Jr. and R. L. Visentin, ''A signal processing view of strip-mapping synthetic aperture radar,'' IEEE Trans. Acoust., Speech, Signal Process. **37**, 2131–2147 (1989).
[15] J. C. Curlander and R. N. McDonough, *Synthetic Aperture Radar*, Wiley Series in Remote Sensing (Wiley, New York, 1991).
[16] C. V. Jakowatz, Jr., D. E. Wahl, P. H. Eichel, D. C. Ghiglia, and P. A. Thompson, *Spotlight-Mode Synthetic Aperture Radar: A Signal Processing Approach* (Kluwer Academic, Boston, 1996).
[17] C. Cafforio, C. Prati, and F. Rocca, ''SAR data focusing using seismic migration techniques,'' IEEE Trans. Aerosp. Electron. Syst. **27**, 194–207 (1991).
[18] M. Soumekh, ''A system model and inversion for synthetic aperture radar imaging,'' IEEE Trans. Image Process. **1**, 64–76 (1992).